

Title: Correcting for T₁ bias in Magnetization Transfer Saturation (MT_{sat}) Maps Using Sparse-MP2RAGE

Authors:

Christopher D. Rowley^{1,2,3}, Mark C. Nelson¹, Jennifer S.W. Campbell¹, Ilana R. Leppert¹, G. Bruce Pike⁴, Christine L. Tardif^{1,2,5}

¹ McConnell Brain Imaging Centre, Montreal Neurological Institute and Hospital, McGill University, Montreal, QC, Canada H3A 2B4

² Department of Neurology and Neurosurgery, McGill University, Montreal, QC, Canada H3A 2B4

³ Department of Physics and Astronomy, McMaster University, Hamilton, ON, Canada L8S 4L8

⁴ Hotchkiss Brain Institute and Departments of Radiology and Clinical Neuroscience, University of Calgary, Calgary, Canada T2N 4N1

⁵ Department of Biomedical Engineering, McGill University, Montreal, QC, Canada H3A 2B4

Competing Interests: There are no competing interests to declare.

Keywords: MRI, magnetization transfer, T1, myelin, macromolecules, brain

Corresponding Author:

Christine Tardif, Department of Biomedical Engineering, McGill University, Montreal, QC, Canada H3A 2B4 christine.tardif@mcgill.ca

Christopher Rowley, Department of Physics and Astronomy, McMaster University, Hamilton, ON, Canada. L8S 4L8

Abstract:

Purpose:

Magnetization transfer saturation (MT_{sat}) mapping is commonly used to examine the macromolecular content of brain tissue. This study compared variable flip angle (VFA) T_1 mapping against compressed sensing (cs)MP2RAGE T_1 mapping for accelerating MT_{sat} imaging.

Methods: VFA, MP2RAGE and csMP2RAGE were compared against inversion recovery (IR) T_1 in a phantom at 3 Tesla. The same 1 mm VFA, MP2RAGE and csMP2RAGE protocols were acquired in four healthy subjects to compare the resulting T_1 and MT_{sat} . Bloch-McConnell simulations were used to investigate differences between the phantom and *in vivo* T_1 results. Finally, ten healthy controls were imaged twice with the csMP2RAGE MT_{sat} protocol to quantify repeatability.

Results: The MP2RAGE and csMP2RAGE protocols were 13.7% and 32.4% faster than the VFA protocol, respectively. All approaches provided accurate T_1 values (<5% difference) in the phantom, but the accuracy of the T_1 times was more impacted by differences in T_2 for VFA than for MP2RAGE. *In vivo*, VFA generated longer T_1 times than MP2RAGE and csMP2RAGE. Simulations suggest that the bias in the T_1 values between VFA and IR-based approaches (MP2RAGE and IR) could be explained by the MT-effects from the inversion pulse. In the test-retest experiment, we found that the csMP2RAGE has a minimum detectable change of 3% for T_1 mapping and 7.9% for MT_{sat} imaging.

Conclusions:

We demonstrated that csMP2RAGE can be used in place of VFA T_1 mapping in an MT_{sat} protocol. Furthermore, a shorter scan time and high repeatability can be achieved using the csMP2RAGE sequence.

Introduction:

Magnetization transfer saturation (MT_{sat}) is a semi-quantitative method that is used commonly as a biomarker for tissue myelin content (Helms et al., 2010, 2008b). The technique uses magnetization transfer (MT) contrast, which is generated using an off-resonance radiofrequency pulse that partially saturates the bound protons in the macromolecular pool. This decreased, or partially saturated, state of magnetization is transferred to the water pool and presents itself as a decrease in MRI-observable signal. While the MT ratio (MTR) is a more simplistic method to investigate these effects, MT_{sat} aims to quantify this saturation while accounting for counteracting effects of T_1 relaxation. The calculation requires an MT-weighted image and knowledge of the observed longitudinal relaxation time ($T_{1\text{obs}}$, shortened herein to T_1) and apparent equilibrium magnetization (M_0).

Typically, the M_0 and T_1 maps for this purpose are generated using a variable flip angle (VFA) experiment (Christensen et al., 1974; Helms et al., 2008b; Venkatesan et al., 1998; Weiskopf et al., 2013). VFA T_1 mapping involves using a spoiled gradient-recalled echo (SPGR) or fast low angle shot (FLASH) sequence to acquire two or more images with different T_1 -weightings, where the timing and flip angles of each image can be optimized for signal-to-noise in the final map (Helms et al., 2011). T_1 values can then be obtained through fitting (Gupta, 1977) or solving signal equations (Helms et al., 2008a). VFA T_1 mapping has been widely adopted due to its ease of use (uses product sequences, simple calculation), and for its ability to generate high-resolution 3D maps much faster than more conventional approaches such as inversion recovery (IR) (see (Kingsley, 1999) for a list of seminal papers on T_1 mapping). It also uses the same base pulse sequence that is used for the MT-weighted image, removing sequence-dependent receiver gain differences, matches geometric distortions and has the same T_2^* contributions due to matching echo times.

However, VFA T_1 mapping has been shown to provide T_1 times up to 20% longer compared to the gold standard IR approach (Stikov et al., 2015b; Tsalios et al., 2017). Post-processing of VFA T_1 maps can correct for flip angle inaccuracies caused by B_1^+ inhomogeneities (ΔB_1^+) (Venkatesan et al., 1998), and for incomplete spoiling of the transverse magnetization between excitation pulses (Baudrexel et al., 2018; Preibisch and Deichmann, 2009). This removes spatial variations that correlate with ΔB_1^+ and typically reduces VFA T_1 times in the brain (Baudrexel et al., 2018), but differences remain (Stikov et al., 2015a). This increase in T_1 will result in decreased MT_{sat} values due to the inverse relationship between the two metrics.

MT_{sat} values are also impacted by ΔB_1^+ . It is possible to remove these effects using an empirically derived factor that corrects ΔB_1^+ induced errors in the MT_{sat} map from the MT-weighted image and the VFA-derived T_1 map (Helms, 2015; Weiskopf et al., 2013). A recent framework has shown that it is possible to correct for the ΔB_1^+ effects in the saturation and excitation pulses separately (Rowley et al., 2021), which would permit the use of other T_1 mapping techniques for generating ΔB_1^+ corrected MT_{sat} maps. To this end, this study explores the use of MP2RAGE T_1 mapping in an MT_{sat} protocol.

The MP2RAGE sequence uses two readout blocks following an inversion pulse, where each readout block typically acquires one plane of k-space, to generate two images with different inversion times. The two acquired images are combined with a lookup table derived from Bloch simulations to extract M_0 and T_1 maps (Marques et al., 2010). MP2RAGE T_1 values have been shown to be in strong agreement with gold standard IR T_1 mapping (Tsalios et al., 2017). This sequence has a decreased dependence on ΔB_1^+ , and no motion differences between the images due to their simultaneous

acquisition. Despite the longer TR necessary with the inclusion of an inversion pulse, the shorter echo-spacing in the readout allows the MP2RAGE sequence to be a more efficient at T_1 mapping than the VFA approach. Compressed sensing approaches have been implemented in quantitative MRI protocols previously, including MT_{sat} using VFA imaging available on Philips scanners (Berg et al., 2022). Here, we explored the use of the Siemens compressed sensing MP2RAGE (csMP2RAGE) (Mussard et al., 2020) product sequence for further accelerating an MT_{sat} protocol.

The overall aim of this work is to acquire fast and accurate MT_{sat} maps using csMP2RAGE instead of VFA to remove T_1 effects. This study compares the accuracy and repeatability of M_0 and T_1 values generated using 2D IR, as well as 3D VFA, MP2RAGE and a csMP2RAGE sequences in a calibrated phantom. Next, we investigate how the three accelerated 3D T_1 mapping methods compare *in-vivo* for generating MT_{sat} maps. We use Bloch-McConnell numerical simulations of the sequences to provide insight into the source of the differences in the observed T_1 times. Finally, we present repeatability results from a test-retest imaging experiment in ten healthy controls using the csMP2RAGE sequence for accelerated MT_{sat} imaging.

Methods:

Data acquisition:

This study was approved by our institutional ethics committee. MR images were acquired using a 3T-PrismaFit scanner (Siemens, Germany) with a 32-channel receive coil. The imaging parameters are included in **Table 1**.

To assess the accuracy of the methods, the ISMRM/NIST system phantom (Stupic et al., 2021) (Premium System Phantom, CaliberMRI, Boulder, Colorado) was imaged. 2D spin echo IR images were acquired over the T_1 (NiCl₂) and T_2 (MnCl₂) plates, where each consists of 14 spheres with varying T_1 and T_2 values (listed in **Table 2**). Only the spheres with T_1 values greater than 300 ms were used in the analysis. Both arrays were used to have more samples within the range of healthy brain tissue (700-1600 ms), and to observe potential biases from different T_2 values. MT data was not acquired in the NIST phantom as the solution in the spheres are aqueous and have no macromolecular-associated MT effects.

For comparing pulse sequences, four healthy adults (aged 29-35 years, three female) were imaged using the same hardware and protocol without the IR T_1 mapping. For the test-retest comparison, ten different healthy adults (aged 20-40 years, four female) were imaged using the identical hardware setup but only with the csMP2RAGE MT_{sat} protocol.

All sequences used the Siemens *prescan normalize* option to generate M_0 maps with minimal receive bias. This normalization process incorporates a calibration scan obtained from the body receive coil to correct the sensitivity profile of the head coil. A gain factor of 2.5 was applied to M_0 maps from the MP2RAGE protocols to match the receiver gain factor of the MT-weighted image. B_1^+ maps were acquired using a fast turboFLASH sequence (Chung et al., 2010).

For *in-vivo* imaging, a T_1 -weighted MPRAGE image was acquired as an anatomical reference with the following parameters: 1 mm isotropic, TR = 2300 ms, TE = 2.98 ms, flip angle = 9 deg, TI = 900 ms, FOV = 256x256x192, and a GRAPPA factor of 2 with 32 reference lines. This was done to allow all images of interest to be registered to a common space.

Data fitting:

Image calculations were done in MATLAB 2021b (www.mathworks.com). Spin echo IR T_1 values were fit using the qMRLab toolbox (Karakuzu et al., 2020) using a shortened TR signal equation (Barral et al., 2010).

MP2RAGE-based M_0 and T_1 maps were fit using a lookup table approach that incorporates ΔB_1^+ . This was done by modifying the original MP2RAGE code (<https://github.com/JosePMarques/MP2RAGE-related-scripts>) to extract a ΔB_1^+ corrected M_0 map from the lookup table, in addition to the T_1 map.

The hMRI toolbox was used to calculate the T_1 values from the VFA data (Tabelow et al., 2019) without the small tip angle approximation (Edwards et al., 2021). For the NIST phantom data, spoiling correction was not applied to VFA metrics due to the wide range of T_2 values. For in-vivo data, the T_1 values were corrected for spoiling imperfections (Preibisch and Deichmann, 2009), which was implemented using code from hMRI toolbox for a T_2 value of 80 ms. This is done by fitting the VFA data to extended phase graph simulations of the sequence (Malik et al., 2018) and was included in our model-based corrected VFA values. The corrected M_0 values were obtained from each of the two images by inputting the ΔB_1^+ corrected T_1 values into the FLASH signal equation (equation 1) and then averaging.

$$S = M_0 \sin(\alpha B_1^+) \frac{1 - \exp(-TR/T_1)}{1 - \cos(\alpha B_1^+) \exp(-TR/T_1)} \quad (1)$$

MT_{sat} maps were computed as in (Helms et al., 2008b) using:

$$MT_{\text{sat},\text{uncor}} = \left(\frac{M_0 \cdot \alpha}{S_{MTw}} - 1 \right) \cdot \frac{TR}{T_1} - \frac{\alpha^2}{2} \quad (2)$$

Where α is the excitation flip angle in the MT-weighted image, S_{MTw} is the MT-weighted signal, and TR is the repetition time of the MT-weighted sequence. For the MT_{sat} values derived from MP2RAGE T_1 maps, a model-based correction was used to correct for ΔB_1^+ (Rowley et al., 2021). This same approach was used for the model-based VFA MT_{sat} values. To compare with what is most frequently found in the literature, a VFA MT_{sat} map was generated using a previously generated empirical correction factor (Helms, 2015; Weiskopf et al., 2013) defined as:

$$MT_{\text{sat},\text{cor}} = MT_{\text{sat},\text{uncorr}} \left(\frac{1 - 0.4}{1 - 0.4 \cdot \Delta B_1^+} \right) \quad (3)$$

Regions of Interest (ROI):

Since the 3D and 2D data were acquired with different resolutions over different regions of the phantom, ROIs were manually delineated for the 2D and 3D data (**Figure 1**). The denoised MP2RAGE UNI image was used for manually delineating a 3D mask for the spheres of interest in the NIST

phantom in ITK-snap (Yushkevich et al., 2016). 2D masks were generated from the $TI = 1000$ ms inversion recovery images of each sphere array. Masks were drawn in the image from the first session, with each sphere as a separate label and registered using ANTS (Avants et al., 2008) to align the mask to the subsequent imaging sessions. To avoid edge artifacts, the registered 3D masks for each session were eroded using a sphere with a radius of four voxels in MATLAB, and the 2D masks were eroded using a disk with a radius of two voxels.

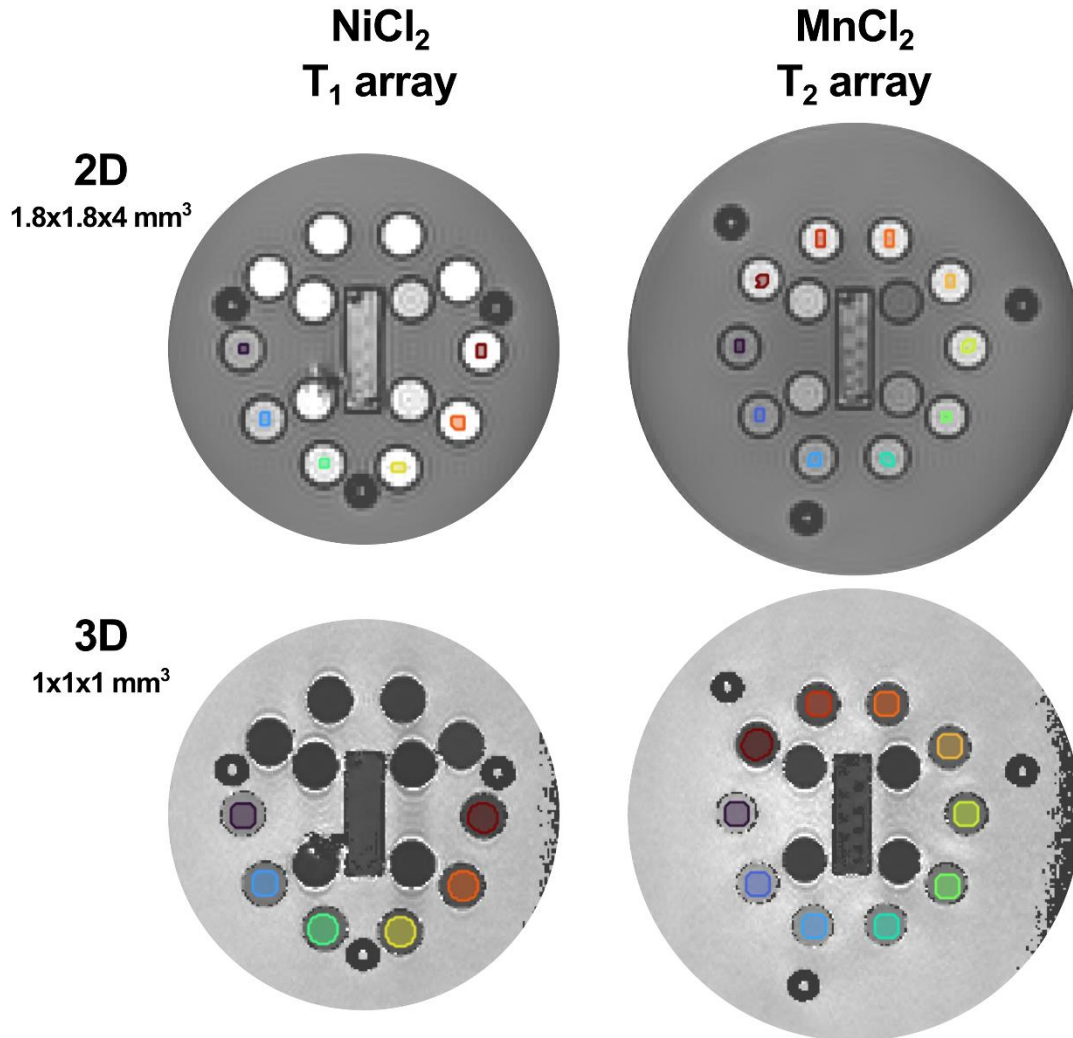


Figure 1: NIST phantom arrays with the ROIs overlaid. Separate ROIs were used for the 2D and 3D images for the T_1 and T_2 sphere plate arrays. ROIs were manually drawn and eroded to avoid edge artifacts.

For the human data, all images were registered to the T_1 -weighted MPRAGE image, which was used as input to the FreeSurfer (v7.2) (Fischl, 2012) *recon-all* pipeline with manual edits to remove dura matter. An ROI analysis was performed utilizing the *wmparc.mgz* segmentation from FreeSurfer for its volumetric white matter (WM) and subcortical gray matter (GM) labels (Desikan et al., 2006). For cortical GM ROIs, the calculated metrics were sampled at the mid-depth cortical surface and averaged over the FreeSurfer *aparc.a2009s* surface ROIs (Destrieux et al., 2010). ROIs were removed with missing data, leaving 89 volumetric ROIs and 75 surface ROIs per subject.

Statistical Analysis:

Metrics were compared using a framework that was recently presented for quantitative imaging of the spinal cord (Lévy et al., 2018). Repeatability (test-retest) was examined in the NIST phantom and ten healthy controls. This involved computing the intraclass correlation coefficient (ICC) and the minimum detectable change (MDC). ICC is the ratio of the inter-subject variance to the total observed variance. This provides insight into the amount of observed variation that is due to genuine between-subject differences compared to variability from the imaging and processing. The MDC defines the minimum necessary difference in a metric needed to report a statistically significant change and is used to assess reliability and the precision of the approach. The MDC is calculated from repeat measurements and is defined as:

$$MDC = \sqrt{2} \cdot 1.96 \cdot \sigma_{within} \quad (4)$$

where σ_{within} is the within subject standard deviation. To assess differences between metrics calculated from different pulse sequences, Bland Altman plots (Altman and Bland, 1983; Giavarina, 2015) were used.

Simulations:

To investigate the MT effect of the different T_1 mapping protocols, simulations of VFA, IR and MP2RAGE sequences were run using code developed for optimizing inhomogeneous MT imaging (Rowley et al., 2023), while following standards set by previous studies. The following tissue parameters were used: $R_{1B} = R_{1A} = R_{1obs} = 1.176 \text{ s}^{-1}$; $M_{0A} = 1$; $k_f = 4.45 \text{ s}^{-1}$; $k_r = 28.34 \text{ s}^{-1}$; $R_{2A} = 12.3 \text{ s}^{-1}$. $R_1 = 1/T_1$, subscripts A and B respectively correspond to free and bound proton pools, subscript obs is the observed R_1 which we will maintain for the simulation section, k is the exchange rate for forward (f) or reverse (r) exchange, and R_{2A} is the transverse relaxation rate of the free protons. There are inconsistencies in the MT literature as to the relationship between R_{1B} , R_{1A} , and R_{1obs} . It is often reported that the value of R_{1B} is poorly fit from traditional qMT experiments (Henkelman et al., 1993), thus we opted to use the convention used by Gloor et al. to set them equal (Gloor et al., 2008). Other studies have fixed these variables in simulations to values that are close to each other (Kim et al., 2014; Teixeira et al., 2019). The relationship previously used by Sled et al., (Henkelman et al., 1993; Sled and Pike, 2001), was derived from the SPGR signal equation and presented an unfair comparison across sequences.

To model the impact of the on-resonance excitation pulses on the bound pool, the absorption of the macromolecular lineshape (typically denoted by variable $g(\Delta)$, where Δ is the offset frequency) was fixed to $1.4e-5 \text{ s}^{-1}$ as in (Gloor et al., 2008; Teixeira et al., 2019). This saturated the bound pool to 88% of its initial value following an inversion pulse as was explicitly set in previous simulations (Kim et al., 2014). Given that methods exist for modeling spoiling imperfections, and therefore could be corrected in post-processing steps, we assumed the signal was perfectly spoiled after each excitation pulse. To investigate the potential impact of MT effects, all tissue parameters were fixed, and the bound pool fraction (M_{0B}) and R_{1obs} varied to examine the MT-related impact of the excitation pulses on the resulting T_1 values. This may overestimate the impact that would be observed in humans *in-vivo*, as tissue parameters are often linked. To investigate the impact that would more likely be observed in healthy tissue, additional simulations were run using linear models that were built from qMT results

reported previously (Sled and Pike, 2001) to modify the variables M_{0B} , k_f , R_{1A} , T_{2A} , and T_{2B} based on the input R_{1obs} (Appendix equations A1-A6).

MATLAB code to calculate the corrected maps and run the simulations are available at <https://github.com/TardifLab/MTsatMP2RAGE>.

Results:

Our main motivation to use csMP2RAGE over VFA for MT_{sat} mapping is to shorten the acquisition protocol. The full MT_{sat} protocol including B_1^+ mapping using csMP2RAGE or MP2RAGE were 32.4% and 13.7% faster than the VFA approach, respectively (see **Table 1**).

All Protocols Provided Accurate T_1 Times in the NIST Phantom

The second objective was to verify the accuracy of these T_1 mapping techniques against reference values and the gold standard IR approach. The NIST phantom provided insight into the accuracy of the T_1 mapping methods in the absence of MT effects, as well as the impact of different T_2 values which may impact spoiling efforts.

MP2RAGE and VFA protocols that fit T_1 based on two measurements, require the sequence timing to be optimized for fitting over a specific range of T_1 values. Outside this range, the fit results can be poor, and this is made apparent in Figure 2A and 2B where the T_1 values below 475 ms are poorly fit in the MP2RAGE scans. From Figures 2A, 2B and 2F, we observe that VFA tends to fit longer T_1 times than IR and MP2RAGE scans. As the two arrays have different T_2 times for similar T_1 ranges, Figures 2C, 2D and 2E provide insight into the T_2 dependence of the fitting compared to the IR approach. The clear separation of the VFA points from the two arrays suggests that this T_1 mapping method is additionally sensitive to parameters outside of T_1 . The MP2RAGE-based values demonstrated increased differences with increasing T_1 values but presented good agreement over the range of T_1 times of the sphere arrays. The repeatability of the metrics was investigated over four sessions and the results are presented in Figure 2G. To better represent the brain, only ROIs with T_1 values above 600 ms were used in this calculation. Despite the offsets of the VFA T_1 values, it had a lower MDC (4.2%) compared to IR (5.8%), MP2RAGE (6.7%) and csMP2RAGE (6.2%). All metrics presented high ICC values (≥ 0.998).

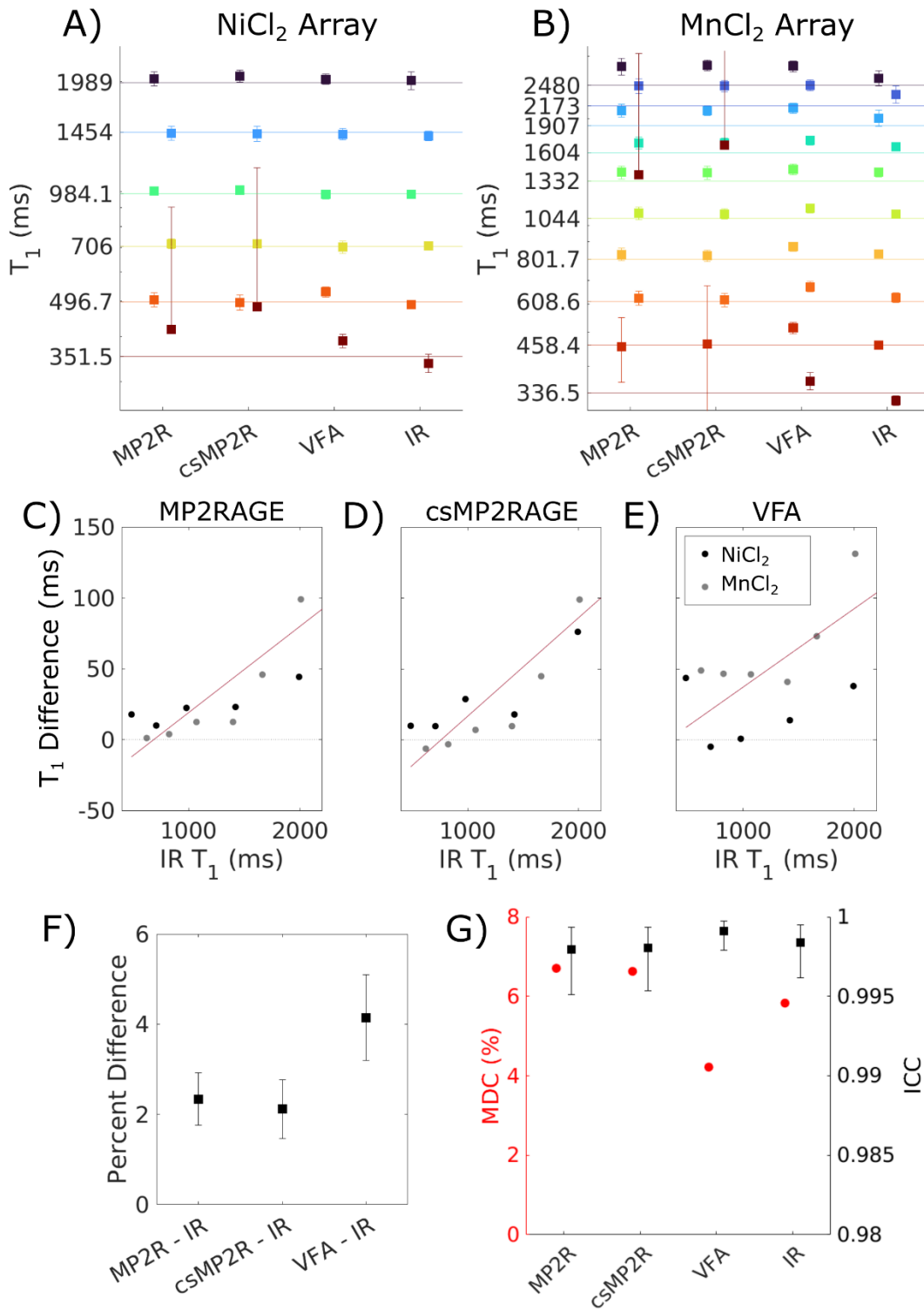


Figure 2: A, B) ROI analysis of NIST phantom spheres from the T₁ and T₂ arrays. Y-axis is log scaled. Data points are the average of the four sessions, horizontal lines mark the reference value for the ROI and the error bars are the standard deviations, colour is matched to ROIs in Figure 1. **C-E)** Shows the difference between accelerated 3D T₁ mapping methods compared to the gold standard 2D IR method. **F)** Average percent difference compared to IR, across all ROIs, averaged over four sessions. **G)** Repeatability analysis from T₁ values acquired over four sessions. VFA provided the most consistent

values in the NIST phantom, presenting the lowest minimum detectable change, and highest intraclass correlation coefficient.

Longer VFA T_1 Times than MP2RAGE Results in Lower MT_{sat} *In Vivo*

Representative maps from a single subject are displayed in **Figure 3**. Visually, there is strong agreement between the M_0 maps. VFA produced longer T_1 times, resulting in lower MT_{sat} values compared to the MP2RAGE-based maps. Minimal additional blurring is observed in the csMP2RAGE map despite the increased acceleration factor.

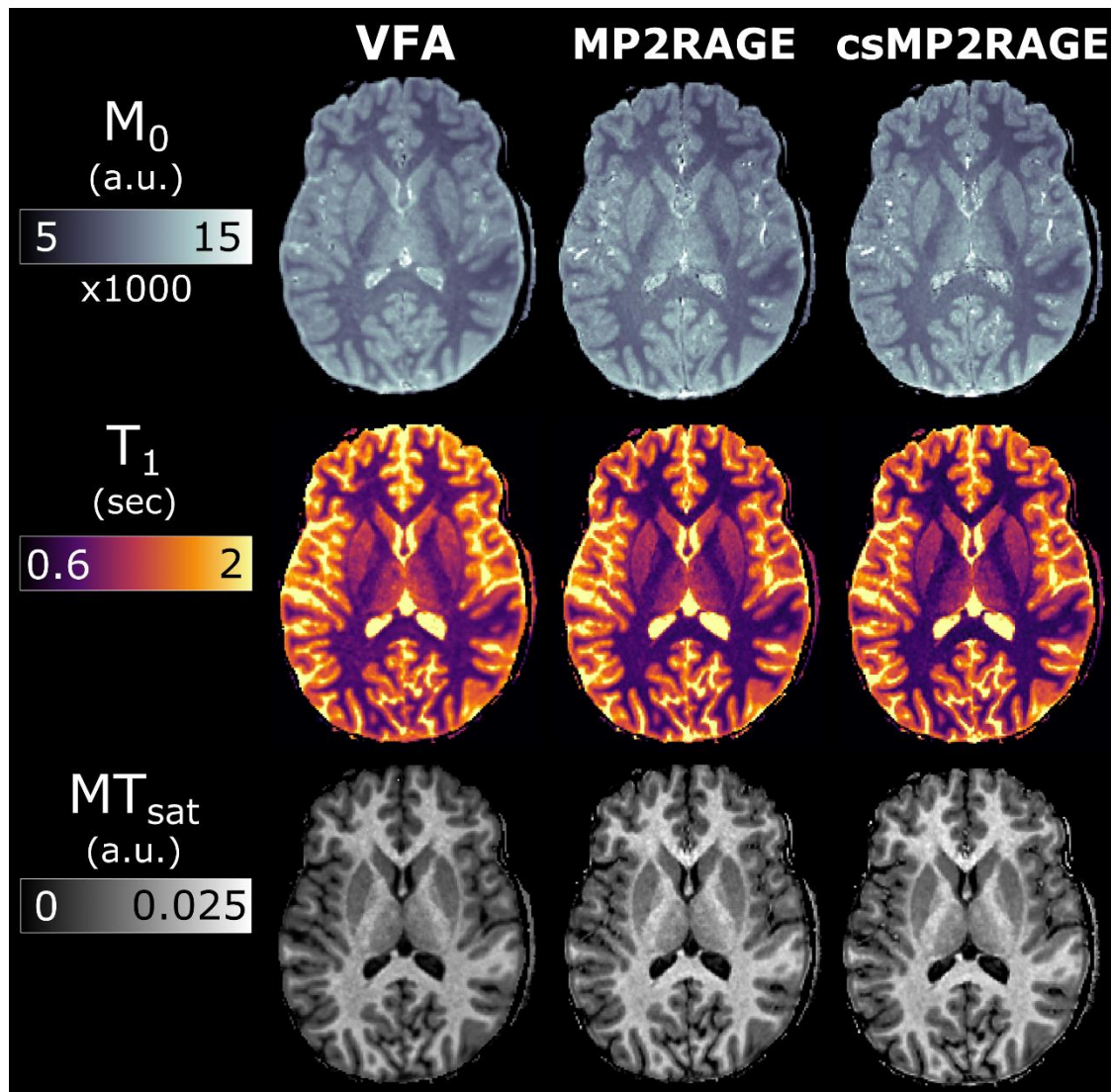


Figure 3: Representative axial slice from a single subject derived from the different T_1 mapping protocols. All maps presented here were corrected for ΔB_1^+ , and the VFA maps were corrected for incomplete spoiling.

The Bland-Altman plots comparing the T_1 and MT_{sat} maps from the three T_1 mapping protocols are presented in **Figure 4**. The VFA approach had a shift of +73 ms in the T_1 values compared to MP2RAGE (Fig. 4A), resulting in a -10.82% offset in the MT_{sat} values (Fig 4D). The trend was similar

when comparing VFA to csMP2RAGE with offsets of +87 ms and -11.78% (Fig. 4B and E). Strong agreement was observed between the MP2RAGE and csMP2RAGE sequences with a calculated difference of -14 ms and +0.965 % for T_1 and MT_{sat} respectively (Fig. 4C and 4F). The difference between metrics appears to have minimal dependence on T_1 in this range of T_1 values.

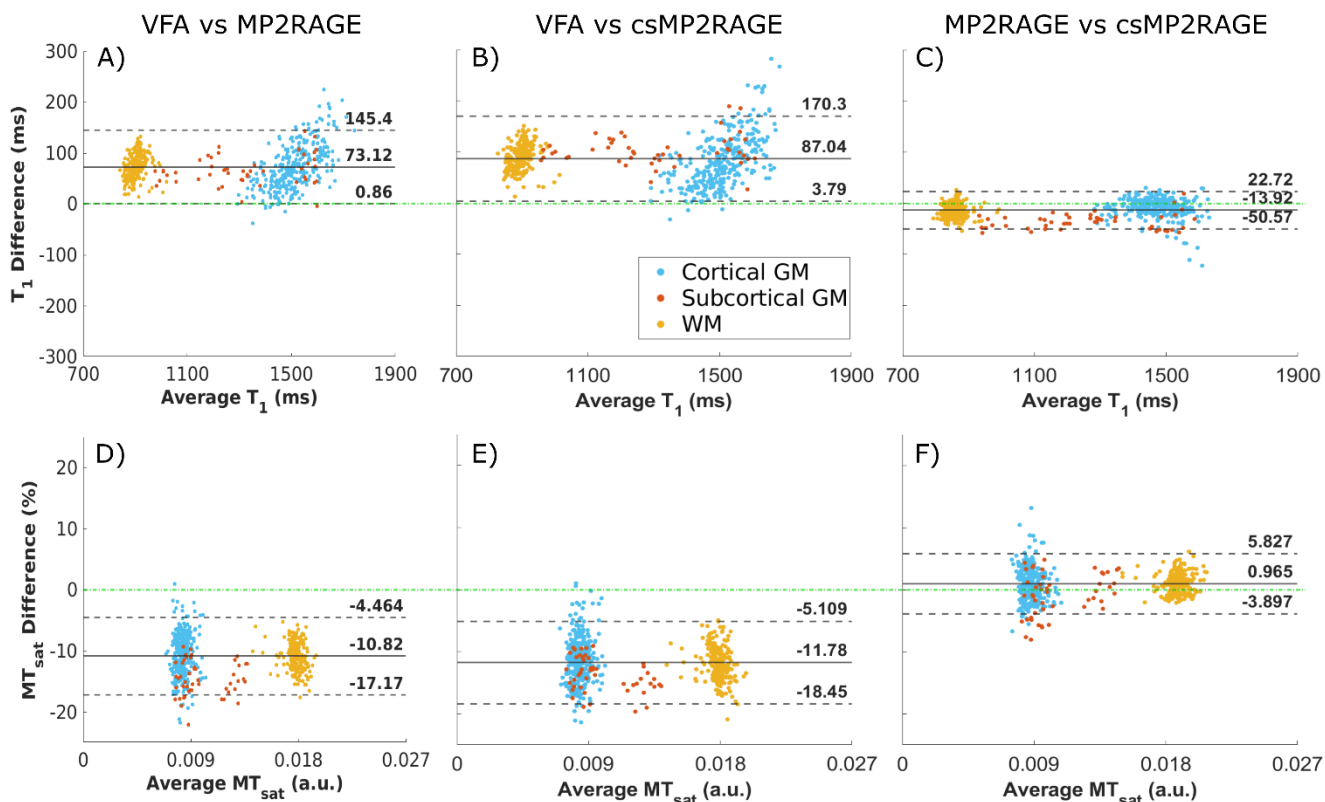


Figure 4: Bland Altman plots to compare T_1 and MT_{sat} values between methods in four subjects. Data points represent the ROI averaged values from four healthy adults. The dashed green line indicates no difference between the metrics. The solid black line indicates the average difference, with the dashed lines representing the 95% confidence interval.

VFA is More Impacted By ΔB_1^+

Reducing scanner-related image variations decreases the MDC of a metric. **Figure 5** highlights the impact of ΔB_1^+ correction on the different maps. There was more variation in the MP2RAGE values caused by ΔB_1^+ than was present between the MP2RAGE and csMP2RAGE from Figure 4. The large spread of values in Figure 5B indicates that ΔB_1^+ correction is necessary for VFA T_1 values. Figure 5D highlights the partial cancellation of ΔB_1^+ effects inherent in the MT_{sat} calculation, where $\pm 30\%$ differences in T_1 reduced to -16% to +6% differences in MT_{sat} .

Finally, we compared the commonly employed empirical correction for MT_{sat} against a model-based approach that included corrections for incomplete spoiling in the T_1 map, which is displayed in Figure 5E. While there is a slight bias towards lower MT_{sat} values (-3.6%) when using the empirical correction, there is a strong agreement between the values after accounting for the bias. This suggests that either approach could be used to achieve a strong decrease in scanner-induced variance in MT_{sat} values.

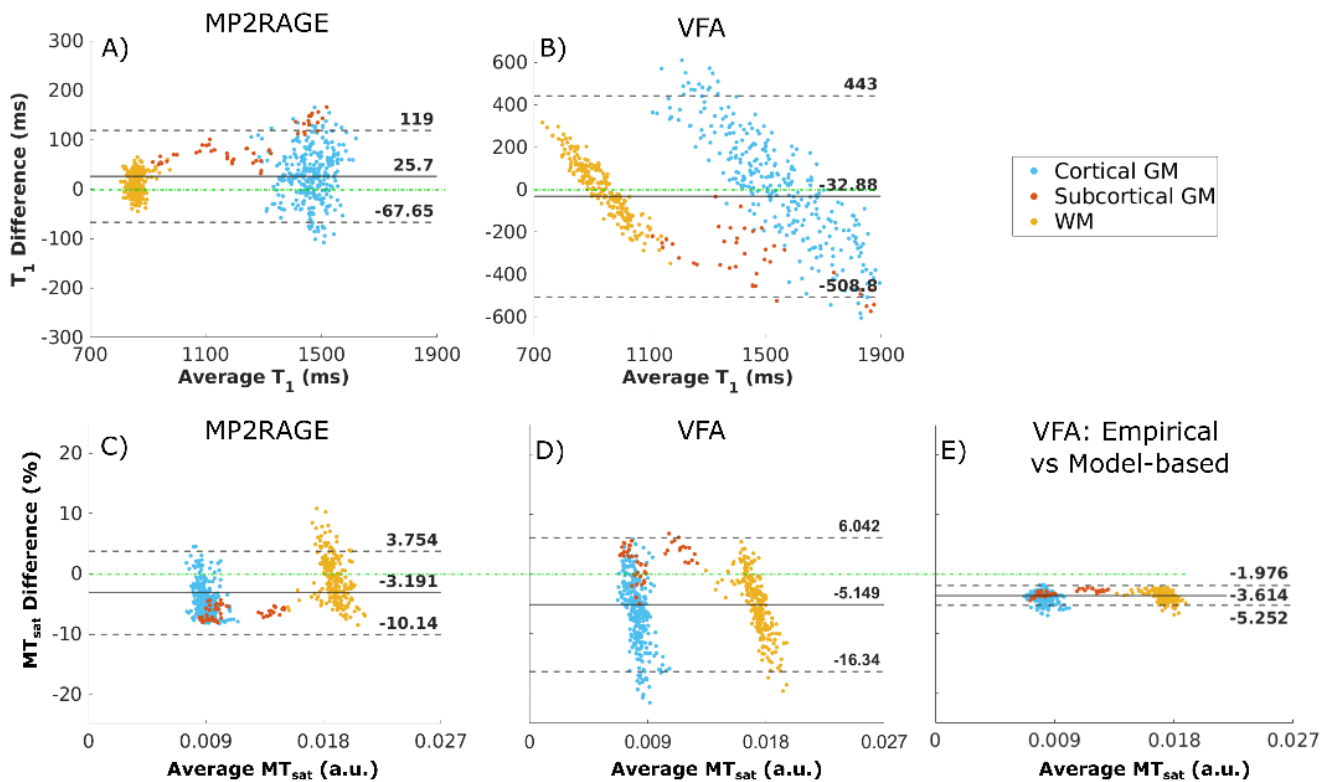


Figure 5: Bland Altman plots compare the results obtained within a method when ΔB_1^+ is corrected for or ignored. This provides an idea of the results based on different processing streams. Note that Plot A and B use different y-axis scaling. Data points represent the ROI averaged values from four healthy adults, the solid black line indicates the average difference, with the dashed lines providing the 95% confidence interval.

Protocol-Dependent MT effects on T₁ Mapping

Modified Bloch-McConnell simulations were used to investigate if MT effects could describe the varying levels of agreement in the T₁ times obtained from the NIST phantom and *in vivo* acquisitions and are presented in **Figure 6**. Plots 6A-6E assume that only T_{1,obs} and M_{0B} are changing. Plots 6A-6C highlight the impact that changes in M_{0B} have on the calculated T_{1,obs} values. The IR and MP2RAGE have larger deviations with increasing M_{0B} than the VFA protocol due to the 180-degree inversion pulse. IR is considered the gold standard for T₁ mapping, and simulations suggest that MP2RAGE can provide values in strong agreement with IR as seen in Figure 6D. MP2RAGE overestimated T_{1,obs} on average by 4% with minimal influence from changes to M_{0B}. VFA values showed little difference compare to IR with M_{0B} = 0, which matches the results from the NIST phantom. Large deviations in output T_{1,obs} (>20%) are noted however with increasing M_{0B} as observed in Figure 6E. As these variables tend to covary in health and in disease, Figure 6F presents simulations if we assume all tissue parameters change as a function of the input ‘true’ T_{1,obs}. A difference of 70 ms is observed between VFA and MP2RAGE corroborating the results presented in Figure 4A. MP2RAGE T₁ times diverge from IR with increasing T₁ and are 20 ms longer than IR at T₁ times typical for WM (~850 ms), and 70 ms longer at T₁ times representative of GM (1400 ms).

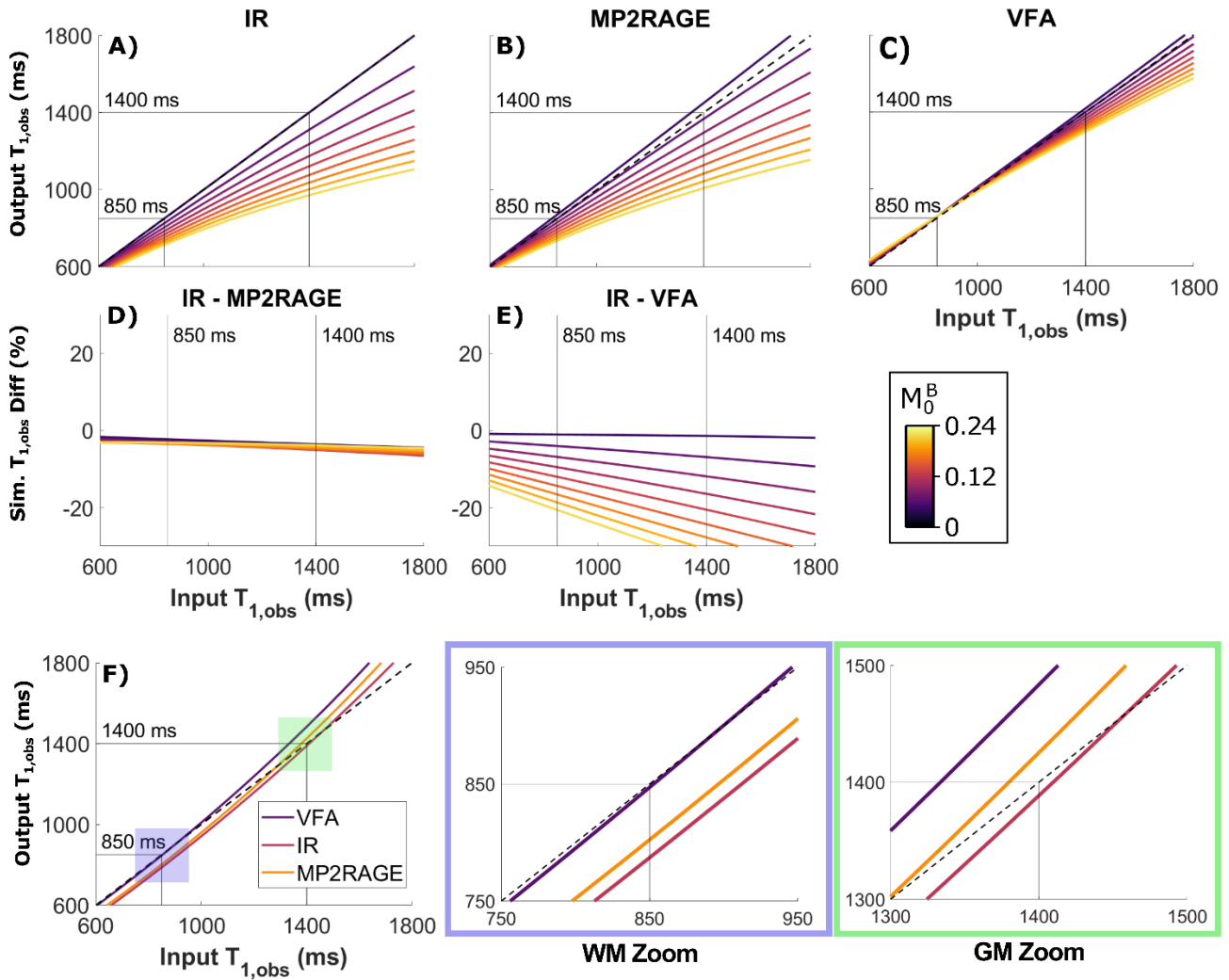


Figure 6: The impact of MT-effects on T_1 values. **A, B)** A strong MT-effect is observed for IR and MP2RAGE methods, arising from the 180-degree inversion pulse. **C)** VFA is impacted by MT-effects to a lesser degree than IR and MP2RAGE. The differences against the gold-standard IR are presented in **D)** and **E)**. **F)** In healthy tissue, multiple tissue parameters tend to change with T_1 . By estimating tissue parameters from the qMT values obtained in (Sled and Pike, 2001), we observe a smaller impact of the MT-effect. An average of 70 ms is observed between VFA and MP2RAGE, and an additional 70 ms between MP2RAGE and IR, which converges at shorter T_1 times. Reference lines indicate typical T_1 values for GM and WM at 3T.

The csMP2RAGE MT_{sat} Protocol Presents Strong Repeatability

Figure 7 presents the test-retest MT_{sat} results using csMP2RAGE for the T_1 mapping protocol in 10 healthy controls. We observe good test-retest values with minimal bias between scans ($<1\%$). T_1 was the most repeatable parameter with an MDC of 2.95%. MT_{sat} presented the largest MDC of 7.88%. A larger value is expected as the errors in the measurement of both M_0 and T_1 propagate through the calculation. If we simulate a realistic input SNR of 70 at 3T, then we expect the calculated MP2RAGE

T_1 map to have an SNR of 55 and the MT_{sat} map to have an SNR of 22 from image noise alone. This represents an SNR decrease of a factor of 2.5, which is close to the value we find *in-vivo* of 2.67, which also includes physiological noise.

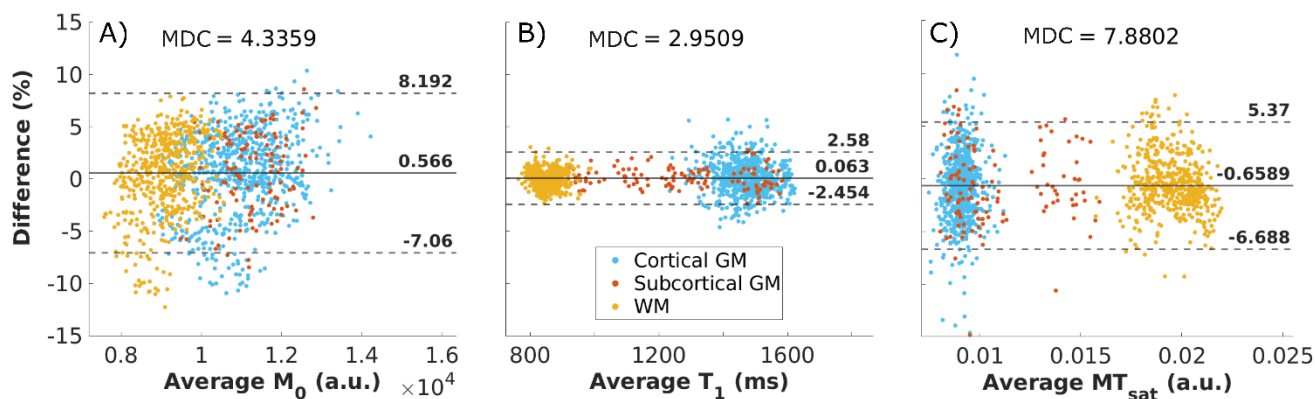


Figure 7: Test-retest ROI analysis using the compressed sensing based MP2RAGE for accelerated MT_{sat} imaging. The solid black line indicates the average difference, and the dashed lines represent 1.96-standard deviation of the difference values, providing the 95% confidence interval. MDC = minimum detectable change.

Discussion:

This study investigated the use of MP2RAGE T_1 mapping for accelerating MT_{sat} imaging. The MP2RAGE T_1 mapping protocol reduced the scan time by 13.7% compared to the VFA protocol, with csMP2RAGE being 32.4% shorter than the VFA protocol. Using the NIST phantom, we found that all approaches could provide accurate T_1 values in aqueous phantoms (less than 5% deviation from reference), but the VFA T_1 values were more impacted by differences in T_2 when not correcting for incomplete spoiling. In vivo, we replicated previous reports of VFA producing larger T_1 values (Stikov et al., 2015b; Tsalios et al., 2017), even when correcting for incomplete spoiling and ΔB_1^+ . ΔB_1^+ correction was shown to have a larger impact on VFA than MP2RAGE T_1 values, and an empirical correction produced comparable results to a model-based ΔB_1^+ correction of MT_{sat} values. Bloch-McConnell simulations suggest that the residual bias in the T_1 values between VFA and IR-based approaches (MP2RAGE and IR) could be explained by the MT-effects from the inversion pulse. Finally, we reported on the MDC from the csMP2RAGE protocol to characterize the ability of this accelerated approach to detect changes.

csMP2RAGE facilitates shorter MT_{sat} acquisition times.

We show that the MT_{sat} protocol can be accelerated using a single MP2RAGE scan instead of acquiring two images needed for VFA T_1 mapping, with additional time saved using csMP2RAGE. Previous work has looked to accelerate the VFA protocol with sparse sampling techniques (Berg et al., 2022; Paajanen et al., 2023; Tamada et al., 2018; Zhang et al., 2015; Zhao et al., 2015). It was shown that a 1 mm isotropic multi-echo MT_{sat} protocol using a compressed sensing VFA protocol could be acquired in 15:40 (min:sec) using a 4x subsampling and in 10:30 with 6x subsampling factor (Berg et al., 2022). This produced high-quality quantitative maps where metric variance increased with acceleration factor, with minimal acceleration-induced bias (Berg et al., 2022). The total protocol using csMP2RAGE in

this study was 10:46 with a 4.6x subsampling factor, with further time savings possible if compressed sensing was used in the MT-weighted image. While this work used cartesian k-space sampling, T_1 mapping can also be accelerated with undersampled non-cartesian trajectories combined with model-based reconstructions (Maier et al., 2019).

It is worth noting that MT_{sat} imaging is typically part of a multi-parametric mapping protocol which also uses multi-echo data for T_2^* fitting (Weiskopf et al., 2013). It is possible to use a multi-echo MP2RAGE sequence to obtain this information as well (Caan et al., 2019; Metere et al., 2017; Sun et al., 2020), however this study focuses on the T_1 -portion of the protocol. In the NIST phantom, the MDC values were lowest in the VFA protocol, and averaging data across echoes could further increase the SNR and lower the MDC. This increase in SNR comes at the cost of additional scan time from the longer TR required to fit the multi-echo readout, where it may be possible to achieve similar MDC values in a time matched MP2RAGE sequence. The time savings offered with the csMP2RAGE, with minimal impact on data quality, permits the generation of MT_{sat} maps in significantly less time. The csMP2RAGE will be beneficial for imaging patient populations where movement might be an issue and/or to make time to acquire complementary data.

On the accuracy of T_1 mapping methods

Strong agreement was observed between the different methods for measuring T_1 in the NIST phantom, with greater differences *in-vivo*. We replicate a previous report showing that MP2RAGE produces T_1 values that are closer to IR values than VFA does (Tsialios et al., 2017). With correction for flip angle inaccuracies, we achieved VFA T_1 values that were similar to IR values in an aqueous phantom (~4% difference), but a larger bias was found *in-vivo* that our simulations suggest is due to MT effects. As we corrected for incomplete spoiling and flip angle inaccuracies *in-vivo*, our simulations assumed perfect spoiling with no flip angle inaccuracies. This resulted in a simulated difference of 70 ms which matched our *in-vivo* results between VFA and MP2RAGE, providing further support for the differences being driven by MT.

IR is considered the gold standard approach for obtaining reference T_1 values. While this may be appropriate for aqueous phantoms, our simulations demonstrate the potentially large impact that the presence of a bound pool can have on the fit T_1 values. Exchange between the bound and free pools is noted as the source of biexponential T_1 recovery (Labadie et al., 2014; Rioux et al., 2016; van Gelderen et al., 2016) leading to decreased T_1 values from an initial faster recovery of magnetization (Mossahebi et al., 2014). Our simulations suggest that this is one reason why VFA mapping may produce elevated T_1 values *in-vivo* compared to the more MT-intensive IR approaches. A previous solution proposed to facilitate inter-study comparisons was to present T_1 values alongside the root mean square B_1^+ ($B_{1\text{rms}}$) of the sequence (Teixeira et al., 2019). Future work could investigate correcting IR-based T_1 mapping methods for MT-effects by including these into the lookup tables. However, this would require the assumption of an increasing number of tissue parameters that may or may not change concurrently. Unexpected tissue variations could lead to greater errors, which could be an important factor when using these methods to study pathologies.

The results of this study suggest that VFA and MP2RAGE can measure repeatable T_1 values at 3T over the expected range of T_1 times of brain tissue. Previous studies have investigated the repeatability of VFA T_1 mapping. In a similar study in the spinal cord, the MDC for VFA-derived T_1 was ~9% (Lévy et al., 2018). Strong repeatability and inter-site reliability values have been exhibited for VFA mapping

using thick slices and four flip angles, which yielded even higher repeatability of their MTR metrics (Schwartz et al., 2019). A reproducibility study of a multi-parameter mapping protocol demonstrated lower intra- and inter-site coefficients of variation in their R_1 metrics compared to MT_{sat} (Leutritz et al., 2020). While we found VFA-derived T_1 values to be most repeatable in a NIST phantom, a previous study found improved accuracy and precision when using IR over VFA, with VFA errors increasing when moving from 1.5T to 3T. Ultimately the repeatability and reproducibility will depend on the hardware and sequence timing used.

The impact of ΔB_1^+ on measured T_1 times

It is well known that VFA T_1 values need to be corrected for ΔB_1^+ (Boudreau et al., 2017; Stikov et al., 2015a) and for incomplete spoiling (Baudrexel et al., 2018; Corbin and Callaghan, 2021; Preibisch and Deichmann, 2009; Yarnykh, 2010). However, many variables that may be unknown to users, such as spoiling parameters, are required to perform these corrections. MP2RAGE is less sensitive to ΔB_1^+ (Marques et al., 2010), but reproducibility can be improved by including ΔB_1^+ in the lookup table (Haast et al., 2021). Our study reinforces these reports with substantially more variation observed between VFA T_1 values with and without ΔB_1^+ correction compared to MP2RAGE. The effects of incomplete spoiling are likely to appear when comparing the T_1 of ROIs with different T_2 values, as spoiling phase increments are optimized for a specific T_2 (Yarnykh, 2010). While MP2RAGE may also suffer from incomplete spoiling issues, our results in the NIST phantom suggest that the magnitude of this effect is greater in the VFA approach. This is due to the idle time in the sequence that permits the formation of the T_1 contrast allowing the transverse magnetization to dissipate.

While this study is largely focused on the T_1 aspects of MT_{sat} imaging, it should be noted that ΔB_1^+ impacts the MT-weighted image and the subsequent MT_{sat} value as well. Correcting for these effects will improve repeatability and reduce the MDC. This was previously addressed by using an empirical factor to correct MT_{sat} values that had no corrections applied during the calculation (Helms, 2015; Weiskopf et al., 2013). These correction factors are derived by generating MT_{sat} maps from images with different transmit field strengths to characterize variations as a function of B_1^+ . Here, we demonstrate that similar results can be achieved using a model-based correction that permits separate correction of T_1 , M_0 , and MT_{sat} values (Rowley et al., 2021). An additional benefit of correcting these effects separately is that it permits the addition of other corrections, such as for incomplete spoiling. Importantly, as shown in this study, it permits the flexibility of using different T_1 mapping techniques to generate MT_{sat} maps that are corrected for ΔB_1^+ without needing to acquire additional data to generate new empirical correction factors. This is important as the acquisition of the necessary data for generating these correction factors can require the use of custom MRI sequences.

The reduced sensitivity of MP2RAGE to ΔB_1^+ effects may also be an important consideration for imaging at 7T, where these variations are larger across the brain. MP2RAGE may be a practical option at ultra-high field as MP2RAGE images are often collected in place of an MPRAGE to obtain a uniform T_1 -weighted anatomical image. Additionally, initial work has demonstrated that MP2RAGE T_1 mapping is more reproducible compared to the VFA approach at 7T using single-channel transmission (sTx) (Voelker et al., 2021). It is possible to reduce ΔB_1^+ using parallel transmission (pTx), however ΔB_1^+ techniques would need to be adjusted to account for the effective spatial dependence of the radiofrequency pulses, particularly for MT-effects.

In conclusion, this study demonstrates that the MP2RAGE sequence can successfully replace the VFA portion of an MT_{sat} protocol to remove the T_1 effects while significantly reducing total scan time. We have quantified the difference between the values obtained from both approaches to facilitate future comparisons across studies using different T_1 mapping methods.

Acknowledgements:

The authors thank Prof. Nikola Stikov and Agah Karakuzu (Polytechnique Montreal) for providing the NIST phantom for this study. The McConnell Brain imaging Centre is supported by Healthy Brains for Healthy Lives, the Brain Canada Foundation, through the Canada Brain Research Fund, with the financial support of Health Canada. This project was funded by the Natural Sciences and Engineering Research Council of Canada, the Fonds de recherche du Québec – Santé, the Campus Alberta Innovates Program, Quebec BioImaging Network, Jeanne Timmins Costello and Dr. David T.W. Lin Fellowships.

References

- Altman, D.G., Bland, J.M., 1983. Measurement in Medicine: The Analysis of Method Comparison Studies. *Stat.* 32, 307–317. <https://doi.org/10.2307/2987937>
- Avants, B.B., Epstein, C.L., Grossman, M., Gee, J.C., 2008. Symmetric diffeomorphic image registration with cross-correlation: Evaluating automated labeling of elderly and neurodegenerative brain. *Med. Image Anal.* 12, 26–41. <https://doi.org/10.1016/j.media.2007.06.004>
- Barral, J.K., Gudmundson, E., Stikov, N., Etezadi-Amoli, M., Stoica, P., Nishimura, D.G., 2010. A robust methodology for in vivo T_1 mapping. *Magn. Reson. Med.* 64, 1057–1067. <https://doi.org/10.1002/mrm.22497>
- Baudrexel, S., Nöth, U., Schüre, J.R., Deichmann, R., 2018. T_1 mapping with the variable flip angle technique: A simple correction for insufficient spoiling of transverse magnetization. *Magn. Reson. Med.* 79, 3082–3092. <https://doi.org/10.1002/mrm.26979>
- Berg, R.C., Leutritz, T., Weiskopf, N., Preibisch, C., 2022. Multi-parameter quantitative mapping of R_1 , R_2^* , PD, and MT_{sat} is reproducible when accelerated with Compressed SENSE. *Neuroimage* 253, 119092. <https://doi.org/10.1016/j.neuroimage.2022.119092>
- Boudreau, M., Tardif, C.L., Stikov, N., Sled, J.G., Lee, W., Pike, G.B., 2017. B_1 mapping for bias-correction in quantitative T_1 imaging of the brain at 3T using standard pulse sequences. *J. Magn. Reson. Imaging* 46, 1673–1682. <https://doi.org/10.1002/jmri.25692>
- Caan, M.W.A., Bazin, P.L., Marques, J.P., de Hollander, G., Dumoulin, S.O., van der Zwaag, W., 2019. MP2RAGEME: T_1 , T_2^* , and QSM mapping in one sequence at 7 tesla. *Hum. Brain Mapp.* 40, 1786–1798. <https://doi.org/10.1002/hbm.24490>
- Christensen, K.A., Grant, D.M., Schulman, E.M., Walling, C., 1974. Optimal determination of relaxation times of Fourier transform nuclear magnetic resonance. Determination of spin-lattice relaxation times in chemically polarized species. *J. Phys. Chem.* 78, 1971–1977. <https://doi.org/10.1021/j100612a022>
- Chung, S., Kim, D., Breton, E., Axel, L., 2010. Rapid B_1 +mapping using a preconditioning RF pulse

- with turboFLASH readout. *Magn. Reson. Med.* 64, 439–446. <https://doi.org/10.1002/mrm.22423>
- Corbin, N., Callaghan, M.F., 2021. Imperfect spoiling in variable flip angle T1 mapping at 7T: Quantifying and minimizing impact. *Magn. Reson. Med.* 86, 693–708. <https://doi.org/10.1002/mrm.28720>
- Desikan, R.S., Ségonne, F., Fischl, B., Quinn, B.T., Dickerson, B.C., Blacker, D., Buckner, R.L., Dale, A.M., Maguire, R.P., Hyman, B.T., Albert, M.S., Killiany, R.J., 2006. An automated labeling system for subdividing the human cerebral cortex on MRI scans into gyral based regions of interest. *Neuroimage* 31, 968–980. <https://doi.org/10.1016/j.neuroimage.2006.01.021>
- Destrieux, C., Fischl, B., Dale, A., Halgren, E., 2010. Automatic parcellation of human cortical gyri and sulci using standard anatomical nomenclature. *Neuroimage* 53, 1–15. <https://doi.org/10.1016/j.neuroimage.2010.06.010>
- Edwards, L., Pine, K., Helms, G., Weiskopf, N., 2021. Rational approximation of the Ernst equation for dual angle R1 mapping revisited: beyond the small flip-angle assumption, in: *Book of Abstracts ESMRMB 2021*. pp. 45–46.
- Fischl, B., 2012. FreeSurfer. *Neuroimage* 62, 774–781. <https://doi.org/10.1016/j.neuroimage.2012.01.021>.FreeSurfer
- Giavarina, D., 2015. Understanding Bland Altman Analysis. *Biochem. Medica* 25, 141–51.
- Gloor, M., Scheffler, K., Bieri, O., 2008. Quantitative magnetization transfer imaging using balanced SSFP. *Magn. Reson. Med.* 60, 691–700. <https://doi.org/10.1002/mrm.21705>
- Gupta, R.K., 1977. A new look at the method of variable nutation angle for the measurement of spin-lattice relaxation times using fourier transform NMR. *J. Magn. Reson.* 25, 231–235. [https://doi.org/10.1016/0022-2364\(77\)90138-X](https://doi.org/10.1016/0022-2364(77)90138-X)
- Haast, R.A.M., Lau, J.C., Ivanov, D., Menon, R.S., Uludağ, K., Khan, A.R., 2021. Effects of MP2RAGE B1+ sensitivity on inter-site T1 reproducibility and hippocampal morphometry at 7T. *Neuroimage* 224. <https://doi.org/10.1016/j.neuroimage.2020.117373>
- Helms, G., 2015. Correction for residual effects of B1 + inhomogeneity on MT saturation in FLASH-based multi-parameter mapping of the brain, in: *Proceedings of the 23rd Annual Meeting of ISMRM, Toronto, Ontario, Canada*. p. 3360.
- Helms, G., Dathe, H., Dechent, P., 2008a. Quantitative FLASH MRI at 3T using a rational approximation of the Ernst equation. *Magn. Reson. Med.* 59, 667–672. <https://doi.org/10.1002/mrm.21542>
- Helms, G., Dathe, H., Kallenberg, K., Dechent, P., 2010. Erratum to: Helms, Dathe, Kallenberg and Dechent, High-resolution maps of magnetization transfer with inherent correction for Rf inhomogeneity and T1 relaxation obtained from 3D FLASH MRI. *Magn Reson Med* 2008 Dec;60(6):1396-1407. *Magn. Reson. Med.* 64, 1856. <https://doi.org/10.1002/mrm.22607>
- Helms, G., Dathe, H., Kallenberg, K., Dechent, P., 2008b. High-resolution maps of magnetization transfer with inherent correction for RF inhomogeneity and T1 relaxation obtained from 3D FLASH MRI. *Magn. Reson. Med.* 60, 1396–1407. <https://doi.org/10.1002/mrm.21732>
- Helms, G., Dathe, H., Weiskopf, N., Dechent, P., 2011. Identification of signal bias in the variable flip angle method by linear display of the algebraic ernst equation. *Magn. Reson. Med.* 66, 669–677.

<https://doi.org/10.1002/mrm.22849>

- Henkelman, R.M., Huang, X., Xiang, Q. -S, Stanisz, G.J., Swanson, S.D., Bronskill, M.J., 1993. Quantitative interpretation of magnetization transfer. *Magn. Reson. Med.* 29, 759–766. <https://doi.org/10.1002/mrm.1910290607>
- Karakuzu, A., Boudreau, M., Duval, T., Boshkovski, T., Leppert, I., Cabana, J.-F., Gagnon, I., Beliveau, P., Pike, G., Cohen-Adad, J., Stikov, N., 2020. qMRLab: Quantitative MRI analysis, under one umbrella. *J. Open Source Softw.* 5, 2343. <https://doi.org/10.21105/joss.02343>
- Kim, T., Shin, W., Kim, S.G., 2014. Fast magnetization transfer and apparent T1 imaging using a short saturation pulse with and without inversion preparation. *Magn. Reson. Med.* 71, 1264–1271. <https://doi.org/10.1002/mrm.24756>
- Kingsley, P.B., 1999. Methods of measuring spin-lattice (T1) relaxation times: An annotated bibliography. *Concepts Magn. Reson.* 11, 243–276. [https://doi.org/10.1002/\(SICI\)1099-0534\(1999\)11:4<243::AID-CMR5>3.0.CO;2-C](https://doi.org/10.1002/(SICI)1099-0534(1999)11:4<243::AID-CMR5>3.0.CO;2-C)
- Labadie, C., Lee, J.H., Rooney, W.D., Jarchow, S., Aubert-Frécon, M., Springer, C.S., Möller, H.E., 2014. Myelin water mapping by spatially regularized longitudinal relaxographic imaging at high magnetic fields. *Magn. Reson. Med.* 71, 375–387. <https://doi.org/10.1002/mrm.24670>
- Leutritz, T., Seif, M., Helms, G., Samson, R.S., Curt, A., Freund, P., Weiskopf, N., 2020. Multiparameter mapping of relaxation (R1, R2*), proton density and magnetization transfer saturation at 3 T: A multicenter dual-vendor reproducibility and repeatability study. *Hum. Brain Mapp.* 41, 4232–4247. <https://doi.org/10.1002/hbm.25122>
- Lévy, S., Guertin, M.C., Khatibi, A., Mezer, A., Martinu, K., Chen, J.I., Stikov, N., Rainville, P., Cohen-Adad, J., 2018. Test-retest reliability of myelin imaging in the human spinal cord: Measurement errors versus region- and aging-induced variations. *PLoS One* 13, 1–25. <https://doi.org/10.1371/journal.pone.0189944>
- Maier, O., Schoormans, J., Schloegl, M., Strijkers, G.J., Lesch, A., Benkert, T., Block, T., Coolen, B.F., Bredies, K., Stollberger, R., 2019. Rapid T1 quantification from high resolution 3D data with model-based reconstruction. *Magn. Reson. Med.* 81, 2072–2089. <https://doi.org/10.1002/mrm.27502>
- Malik, S.J., Teixeira, R.P.A.G., Hajnal, J. V., 2018. Extended phase graph formalism for systems with magnetization transfer and exchange. *Magn. Reson. Med.* 80, 767–779. <https://doi.org/10.1002/mrm.27040>
- Marques, J.P., Kober, T., Krueger, G., van der Zwaag, W., Van de Moortele, P.F., Gruetter, R., 2010. MP2RAGE, a self bias-field corrected sequence for improved segmentation and T1-mapping at high field. *Neuroimage* 49, 1271–1281. <https://doi.org/10.1016/j.neuroimage.2009.10.002>
- Metere, R., Kober, T., Möller, H.E., Schäfer, A., 2017. Simultaneous quantitative MRI mapping of T1, T2* and magnetic susceptibility with Multi-Echo MP2RAGE. *PLoS One* 12, 1–28. <https://doi.org/10.1371/journal.pone.0169265>
- Mossahebi, P., Yarnykh, V.L., Samsonov, A., 2014. Analysis and correction of biases in cross-relaxation MRI due to biexponential longitudinal relaxation. *Magn. Reson. Med.* 71, 830–838. <https://doi.org/10.1002/mrm.24677>
- Mussard, E., Hilbert, T., Forman, C., Meuli, R., Thiran, J.P., Kober, T., 2020. Accelerated MP2RAGE

- imaging using Cartesian phyllotaxis readout and compressed sensing reconstruction. *Magn. Reson. Med.* 84, 1881–1894. <https://doi.org/10.1002/mrm.28244>
- Paajanen, A., Hanhela, M., Hänninen, N., Nykänen, O., Kolehmainen, V., Nissi, M.J., 2023. Fast Compressed Sensing of 3D Radial T1 Mapping with Different Sparse and Low-Rank Models. *J. Imaging* 9, 151. <https://doi.org/10.3390/jimaging9080151>
- Preibisch, C., Deichmann, R., 2009. Influence of RF spoiling on the stability and accuracy of T1 mapping based on spoiled FLASH with varying flip angles. *Magn. Reson. Med.* 61, 125–135. <https://doi.org/10.1002/mrm.21776>
- Rioux, J.A., Levesque, I.R., Rutt, B.K., 2016. Biexponential longitudinal relaxation in white matter: Characterization and impact on T1 mapping with IR-FSE and MP2RAGE. *Magn. Reson. Med.* 75, 2265–2277. <https://doi.org/10.1002/mrm.25729>
- Rowley, C.D., Campbell, J.S.W., Leppert, I.R., Nelson, M.C., Pike, G.B., Tardif, C.L., 2023. Optimization of acquisition parameters for cortical inhomogeneous magnetization transfer (ihMT) imaging using a rapid gradient echo readout. *Magn. Reson. Med.* 1–14. <https://doi.org/10.1002/mrm.29754>
- Rowley, C.D., Campbell, J.S.W., Wu, Z., Leppert, I.R., Rudko, D.A., Pike, G.B., Tardif, C.L., 2021. A Model-based Framework for Correcting B1+ Inhomogeneity Effects in Magnetization Transfer Saturation and Inhomogeneous Magnetization Transfer Saturation Maps. *Magn. Reson. Med.* 86, 2192–2207. <https://doi.org/10.1002/mrm.28831>
- Schwartz, D.L., Tagge, I., Powers, K., Ahn, S., Bakshi, R., Calabresi, P.A., Todd Constable, R., Grinstead, J., Henry, R.G., Nair, G., Papinutto, N., Pelletier, D., Shinohara, R., Oh, J., Reich, D.S., Sicotte, N.L., Rooney, W.D., 2019. Multisite reliability and repeatability of an advanced brain MRI protocol. *J. Magn. Reson. Imaging* 50, 878–888. <https://doi.org/10.1002/jmri.26652>
- Sled, J.G., Pike, B.G., 2001. Quantitative imaging of magnetization transfer exchange and relaxation properties in vivo using MRI. *Magn. Reson. Med.* 46, 923–931. <https://doi.org/10.1002/mrm.1278>
- Stikov, N., Boudreau, M., Levesque, I.R., Tardif, C.L., Barral, J.K., Pike, G.B., 2015a. On the accuracy of T1 mapping: Searching for common ground. *Magn. Reson. Med.* 73, 514–522. <https://doi.org/10.1002/mrm.25135>
- Stikov, N., Campbell, J.S.W., Stroh, T., Lavelée, M., Frey, S., Novek, J., Nuara, S., Ho, M.K., Bedell, B.J., Dougherty, R.F., Leppert, I.R., Boudreau, M., Narayanan, S., Duval, T., Cohen-Adad, J., Picard, P.A., Gasecka, A., Côté, D., Pike, G.B., 2015b. In vivo histology of the myelin g-ratio with magnetic resonance imaging. *Neuroimage* 118, 397–405. <https://doi.org/10.1016/j.neuroimage.2015.05.023>
- Stupic, K.F., Ainslie, M., Boss, M.A., Charles, C., Dienstfrey, A.M., Evelhoch, J.L., Finn, P., Gimbutas, Z., Gunter, J.L., Hill, D.L.G., Jack, C.R., Jackson, E.F., Karaulanov, T., Keenan, K.E., Liu, G., Martin, M.N., Prasad, P. V., Rentz, N.S., Yuan, C., Russek, S.E., 2021. A standard system phantom for magnetic resonance imaging. *Magn. Reson. Med.* 86, 1194–1211. <https://doi.org/10.1002/mrm.28779>
- Sun, H., Cleary, J.O., Glarin, R., Kolbe, S.C., Ordidge, R.J., Moffat, B.A., Pike, G.B., 2020. Extracting more for less: multi-echo MP2RAGE for simultaneous T1-weighted imaging, T1 mapping, R2* mapping, SWI, and QSM from a single acquisition. *Magn. Reson. Med.* 83, 1178–1191. <https://doi.org/10.1002/mrm.27975>

- Tabelow, K., Balteau, E., Ashburner, J., Callaghan, M.F., Draganski, B., Helms, G., Kherif, F., Leutritz, T., Lutti, A., Phillips, C., Reimer, E., Ruthotto, L., Seif, M., Weiskopf, N., Ziegler, G., Mohammadi, S., 2019. hMRI – A toolbox for quantitative MRI in neuroscience and clinical research. *Neuroimage* 194, 191–210. <https://doi.org/10.1016/j.neuroimage.2019.01.029>
- Tamada, D., Wakayama, T., Onishi, H., Motosugi, U., 2018. Multiparameter estimation using multi-echo spoiled gradient echo with variable flip angles and multicontrast compressed sensing. *Magn. Reson. Med.* 80, 1546–1555. <https://doi.org/10.1002/mrm.27151>
- Teixeira, R.P.A.G., Malik, S.J., Hajnal, J. V., 2019. Fast quantitative MRI using controlled saturation magnetization transfer. *Magn. Reson. Med.* 81, 907–920. <https://doi.org/10.1002/mrm.27442>
- Tsialios, P., Thrippleton, M., Glatz, A., Pernet, C., 2017. Evaluation of MRI sequences for quantitative T1 brain mapping. *J. Phys. Conf. Ser.* 931, 012038. <https://doi.org/10.1088/1742-6596/931/1/012038>
- van Gelderen, P., Jiang, X., Duyn, J.H., 2016. Effects of magnetization transfer on T1 contrast in human brain white matter. *Neuroimage* 128, 85–95. <https://doi.org/10.1016/j.neuroimage.2015.12.032>
- Venkatesan, R., Lin, W., Haacke, E.M., 1998. Accurate determination of spin-density and T1 in the presence of RF- field inhomogeneities and flip-angle miscalibration. *Magn. Reson. Med.* 40, 592–602. <https://doi.org/10.1002/mrm.1910400412>
- Voelker, M.N., Kraff, O., Goerke, S., Laun, F.B., Hanspach, J., Pine, K.J., Ehes, P., Zaiss, M., Liebert, A., Straub, S., Eckstein, K., Robinson, S., Nagel, A.N., Stefanescu, M.R., Wollrab, A., Klix, S., Felder, J., Hock, M., Bosch, D., Weiskopf, N., Speck, O., Ladd, M.E., Quick, H.H., 2021. The traveling heads 2.0: Multicenter reproducibility of quantitative imaging methods at 7 Tesla. *Neuroimage* 232, 117910. <https://doi.org/10.1016/j.neuroimage.2021.117910>
- Weiskopf, N., Suckling, J., Williams, G., Correia, M.M., Inkster, B., Tait, R., Ooi, C., Bullmore, E.T., Lutti, A., 2013. Quantitative multi-parameter mapping of R1, PD*, MT, and R2* at 3T: a multi-center validation. *Front. Neurosci.* 7, 1–11. <https://doi.org/10.3389/fnins.2013.00095>
- Yarnykh, V.L., 2010. Optimal radiofrequency and gradient spoiling for improved accuracy of T1 and B1 measurements using fast steady-state techniques. *Magn. Reson. Med.* 63, 1610–1626. <https://doi.org/10.1002/mrm.22394>
- Yushkevich, P.A., Gao, Y., Gerig, G., 2016. ITK-SNAP: An interactive tool for semi-automatic segmentation of multi-modality biomedical images, in: *Proceedings of the Annual International Conference of the IEEE Engineering in Medicine and Biology Society, EMBS. IEEE*, pp. 3342–3345. <https://doi.org/10.1109/EMBC.2016.7591443>
- Zhang, T., Pauly, J.M., Levesque, I.R., 2015. Accelerating parameter mapping with a locally low rank constraint. *Magn. Reson. Med.* 73, 655–661. <https://doi.org/10.1002/mrm.25161>
- Zhao, B., Lu, W., Hitchens, T.K., Lam, F., Ho, C., Liang, Z.P., 2015. Accelerated MR parameter mapping with low-rank and sparsity constraints. *Magn. Reson. Med.* 74, 489–498. <https://doi.org/10.1002/mrm.25421>

Tables:

Parameter	VFA (PDw/T1w)	MP2RAGE	csMP2RAGE	MT-weighted GRE	B ₁ ⁺ -map	Spin Echo IR
TR (ms)	27/15	5000	5000	27	20 000	2000
Flip Angle (degrees)	6/20	4/5	4/5	6	8	90
Acceleration	6/8 Partial Fourier + GRAPPA 2	6/8 Partial Fourier + GRAPPA 3	4.6x Upsampling, density = 0.5, jitter radius = 1.2, 20 iterations, 6e-4 reg	6/8 Partial Fourier + GRAPPA 2	NA	None
TE (ms)	2.76	2.76	2.66	2.76	2.22	8.5
FOV	224 x 176	256 x 208	256 x 208	224 x 176	96x96x45	224x224
Voxel Size (mm)	1x1x1	1x1x1	1x1x1	1x1x1	2.5x2.5x3	1.8x1.8x4
Turbo factor	1	208	175	1	96	1
TI (ms)	NA	940/2830	940/2830	NA	NA	30, 250, 500, 750, 1000, 1500
MT-parameters	NA	NA	NA	12 ms Gaussian, Δ = 2 kHz B _{1rms} = 3.26 μT	NA	NA
Acquisition Time (min:sec)	5:58/3:20 [total 9:18]	7:07	4:18	5:58	0:40	4:12
Total MT _{sat} Protocol time	15:56	13:45	10:46			

Table 1: Imaging parameters

T₁ array (NiCl₂)		T₂ array (MnCl₂)	
T ₁ (ms)	T ₂ (ms)	T ₁ (ms)	T ₂ (ms)
1989	1465	2480	581.3
1454	1076	2173	403.5
984.1	717.9	1907	278.1
706	510.1	1604	190.94
496.7	359.6	13332	133.27
351.5	255.5	1044	96.89
		801.7	64.07
		608.6	46.42
		458.4	31.97
		336.5	22.56

Table 2: NIST phantom reference values:

Appendix:

Linear Models for Estimating Tissue Parameters in Simulations

The following equations were used for the simulations presented in Figure 6F. These are based on the values in Table 3 in (Sled and Pike, 2001). An exponential relationship was used between M_{0B} and R_{1obs} to prevent negative values over this range.

$$M_{0B} = 0.06732 \cdot R_{1obs}^{1.569} \quad (A1)$$

$$R_{1A} = 1.135 \cdot R_{1obs} - 0.1412 \quad (A2)$$

$$T_{2A} = -0.02915 \cdot R_{1obs} + 0.08381 \quad (A3)$$

$$T_{2B} = 2.166 \cdot 10^{-6} \cdot R_{1obs} + 8.323 \cdot 10^{-6} \quad (A4)$$

$$k_f = 2.898 \cdot R_{1obs} - 0.5081 \quad (A5)$$

$$k_r = k_f / M_{0B} \quad (A6)$$